Journal of Biomedical Optics

SPIEDigitalLibrary.org/jbo

Combined fluorescence and reflectance spectroscopy for *in vivo* quantification of cancer biomarkers in low- and high-grade glioma surgery

Pablo A. Valdés
Anthony Kim
Frederic Leblond
Olga M. Conde
Brent T. Harris
Keith D. Paulsen
Brian C. Wilson
David W. Roberts

SPIE

Combined fluorescence and reflectance spectroscopy for *in vivo* quantification of cancer biomarkers in low- and high-grade glioma surgery

Pablo A. Valdés,[a,b,g] Anthony Kim,[c] Frederic Leblond,[a] Olga M. Conde,[d] Brent T. Harris,[e] Keith D. Paulsen,[a,f] Brian C. Wilson,[c] and David W. Roberts[f,g]
[a]Dartmouth College, Thayer School of Engineering, Hanover, New Hampshire 03755
[b]Dartmouth College, Dartmouth Medical School, Hanover, New Hampshire 03755
[c]University of Toronto, Ontario Cancer Institute, 610 University Avenue, Toronto, Ontario M5G 2M9, Canada
[d]University of Cantabria, Photonics Engineering Group, Avda. de los Castros S/N, Santander 39005, Spain
[e]Georgetown University Medical Center, Department of Pathology and Neurology, 4000 Reservoir Road, NW, Building D, Room 207, Washington, DC 20057
[f]Georgetown University Medical Center, Norris Cotton Cancer Center; 4000 Reservoir Road, NW, Building D, Room 207, Washington, DC 20057
[g]Dartmouth-Hitchcock Medical Center, Section of Neurosurgery, Lebanon, New Hampshire 03756

Abstract. Biomarkers are indicators of biological processes and hold promise for the diagnosis and treatment of disease. Gliomas represent a heterogeneous group of brain tumors with marked intra- and inter-tumor variability. The extent of surgical resection is a significant factor influencing post-surgical recurrence and prognosis. Here, we used fluorescence and reflectance spectral signatures for *in vivo* quantification of multiple biomarkers during glioma surgery, with fluorescence contrast provided by exogenously-induced protoporphyrin IX (PpIX) following administration of 5-aminolevulinic acid. We performed light-transport modeling to quantify multiple biomarkers indicative of tumor biological processes, including the local concentration of PpIX and associated photoproducts, total hemoglobin concentration, oxygen saturation, and optical scattering parameters. We developed a diagnostic algorithm for intra-operative tissue delineation that accounts for the combined tumor-specific predictive capabilities of these quantitative biomarkers. Tumor tissue delineation achieved accuracies of up to 94% (specificity = 94%, sensitivity = 94%) across a range of glioma histologies beyond current state-of-the-art optical approaches, including state-of-the-art fluorescence image guidance. This multiple biomarker strategy opens the door to optical methods for surgical guidance that use quantification of well-established neoplastic processes. Future work would seek to validate the predictive power of this proof-of-concept study in a separate larger cohort of patients.
 [DOI: 10.1117/1.3646916]

Keywords: 5-aminolevulinic acid; protoporphyrin IX; fluorescence-guided resection; optical spectroscopy; glioma; cancer biomarkers.

Paper 11233RR received May 11, 2011; revised manuscript received Sep. 12, 2011; accepted for publication Sep. 16, 2011; published online Oct. 26, 2011.

1 Introduction

Gliomas are the most common of primary brain tumors, accounting for over 60% of all cases. More efficient and accurate tumor detection can improve diagnosis and lead to advances in the treatment and management of disease.[1–5] Biomarkers hold therapeutic and diagnostic promise, in particular, those for intraoperative tumor detection[4–7] during surgeries in which the extent of resection is a significant factor influencing prognosis and local recurrence of disease.[3,8–10]

Optical methods offer a wide range of detection technologies and strategies that exploit tumor-specific optical biomarkers that have the potential to improve intra-operative tumor identification for guiding surgical intervention. For example, high-grade gliomas accumulate the endogenous biomarker protoporphyrin IX (PpIX) following exogenous administration of 5-aminolevulinic acid (ALA), resulting in increased tumor tissue fluorescence. Despite considerable success with PpIX in guiding the resection of these tumors, current fluorescence detection has suffered from low sensitivity, likely due to the relatively low intensity of fluorescence signals and the subjective assessment relative to a complex tissue background. Sensitivity limitations lead to incomplete tumor detection, i.e., resectable tumor tissue is left undetected, which may be the main reason that resulting ALA-induced PpIX fluorescence imaging has only been useful for tumor subtypes that accumulate relatively high PpIX concentrations (i.e., high grade gliomas).[4,7,10–14] We recently reported quantitative measurements of *in vivo* PpIX concentrations in human brain tumors that showed that diagnostically significant levels do occur across a range of intracranial tumor histologies (including low- and high-grade gliomas, meningiomas, and metastases) even when not visibly evident to the surgeon. Despite the improvement in diagnostic accuracy to a degree comparable to that of visible fluorescence for high grade disease, the performance in lower grade gliomas needs further improvement.[7] Nonetheless, these data demonstrated for the first time that ALA-induced PpIX fluorescence has the potential to improve surgery even for low-grade gliomas.

Address all correspondence to: Pablo A. Valdes, Dartmouth College, Thayer School of Engineering, 8000 Cummings Hall, Hanover, New Hampshire 03755. Tel: (603) 410 7225; Fax: (603) 646 3699; E-mail: Pablo.A.Valdes@Dartmouth.edu.

1083-3668/2011/16(11)/116007/14/$25.00 © 2011 SPIE

Neoplastic processes, e.g., metabolic-profile changes, abnormal vasculature formation, tissue hypoxia, increased cellular proliferation, and differential gene expression profiles, provide a variety of potential biomarker targets.[2,4,5,15–17] However, inter- and intra-tumor differences coupled to current technological limitations, have diluted the potential of these biomarkers for *in vivo* tumor detection. Furthermore, the multifaceted characteristics of tumor biology and glioma pathophysiology suggest that any single biomarker is unlikely to provide the required specificity and sensitivity for universal tumor tissue identification. Here, we measured multiple optical chromophores/fluorophores and scattering parameters *in vivo* that are potentially predictive of neoplastic processes and combined them in an algorithm for tumor identification during glioma resection surgery with a diagnostic performance that is superior to intraoperative fluorescence state-of-the-art imaging. The measured quantities comprised total hemoglobin, oxygen saturation, and optical scattering (related to tissue microstructure) derived from the optical reflectance spectra, and concentration of PpIX and associated photoproducts (related to cell metabolism) determined from the quantitative fluorescence spectra. We believe that combining this information into a single diagnostic indicator provides a more comprehensive biologically relevant approach to intraoperative optical tumor tissue detection. Although the data reported here is promising, future studies are required to validate the predictive power of the algorithm on a much larger cohort of patients.

2 Materials and Methods

2.1 *Patient Selection*

The Dartmouth-Hitchcock Medical Center Committee for the Protection of Human Subjects approved this study under a fluorescence-guided brain tumor resection protocol.[7,12,18] All patients participated under informed consent. Patients with a diagnosis of low-grade glioma (LGG), high-grade glioma (HGG), or recurrent glioma (RCG) were administered an oral dose (20 mg/kg body weight) of ALA (DUSA Pharmaceuticals, Tarrytown, New York) dissolved in 100 ml of water approximately three hours prior to the induction of anesthesia. High-resolution post-gadolinium injection pre-operative T1- or T2-weighted magnetic resonance images were acquired and used for standard neuronavigation.

2.2 *Surgical Procedure*

The patient was prepared for intracranial tumor resection following standard practice.[12] The head was spatially registered with the pre-operative magnetic resonance images using a StealthStation Treon (Medtronic, Louisville, Colorado) for image-guided neuronavigation, which relates the position of the focal point of the surgical microscope to the surgical field and image-space coordinates. A Zeiss OPMI Pentero (Carl Zeiss Surgical, GmbH, Oberkochen, Germany) microscope, modified for blue light (fluorescence) imaging, allowed the surgeon to rapidly switch between white-light and fluorescence modes during the procedure. The microscope is equipped with a 400-nm blue light source for PpIX fluorescence excitation; detection is achieved using a three-chip CCD camera, in front of which optical interference filters are placed. PpIX has a fairly broad fluorescence emission in the red region of the spectrum and a relatively low quantum efficiency (<0.01), and this instrumentation allows real-time fluorescence images to be acquired within the spectral range from 620 to 710 nm.

At various times during resection, the surgeon switched from white light to blue light to visualize fluorescence.[7,12,18] The coregistered operating microscope was then focused on a point of interest for optical and tissue sampling. Digital images were recorded in both white- and blue-light modes and a biopsy specimen was acquired at the same location (i.e., focal point of the coregistered operating microscope). Immediately prior to digital image and biopsy acquisition, the surgeon irrigated the location of the intended specimen to ensure clearing of blood and debris, placed the intraoperative fluorescence/reflectance probe at the focal point of the operating microscope (see Sec. 2.3), and performed readings (<0.5 s per acquisition) of the fluorescence and diffuse reflectance spectra in triplicate.[7] Each biopsy site was assigned a qualitative visible fluorescence score from 0 to 4 (0 = no visible fluorescence, 1 = minimal fluorescence, 2 = moderate fluorescence, 3 = high fluorescence, 4 = very high fluorescence) based on the subjective impression of the surgeon of the visible fluorescence before tissue removal. The surgeon (D. W. Roberts) had experience in using this fluorescence imaging system on over 70 patients. Biopsy samples were collected at the beginning, middle, and end of resection from areas that displayed both visible (red) fluorescence contrast (if present), as well as nonvisible fluorescent regions that were part of the planned resection volume. Control data were also acquired in each case consisting of spectroscopic measurements in normal brain without a corresponding biopsy.

The biopsy specimens were separated into three equal parts for further processing: one part was placed in formalin, one in optimal cutting temperature compound and frozen in liquid nitrogen, and the final part was placed in a cryogenic vial and frozen in liquid nitrogen. Methodological details can be found in Valdes et al.[7]

2.3 *In Vivo Optical Probe Measurements and Quantification*

An intra-operative hand-held optical probe was used to provide the surgeon with quantitative *in vivo* and *in situ* pathophysiological data that is complementary to the qualitative fluorescence information derived from the state-of-the-art neurosurgical microscope described in Sec. 2.2.

2.3.1 *Instrumentation*

The spectroscopic probe developed for intraoperative fluorescence and diffuse reflectance measurements[7,19,20] (A. Kim and B. C. Wilson) is illustrated in Fig. 1. It is comprised of four optical fibers linearly arranged at the tip and 260 μm apart (center-to-center). Two fibers act as white light sources located $d = 260$ and 520 μm apart from a third detection fiber. The latter is connected to a spectrometer (USB2000 + : OceanOptics, Dunedin, Florida) with 0.35 nm spectral resolution. The fourth fiber serves as a blue light source located at $d = 260$ μm from the detector fiber. Each fiber consists of a 200-μm diameter silica core with a numerical aperture of 0.22. The fibers were bundled into an 18-gauge stainless steel shaft forming the tissue-contact end of the probe and connected to a software-controlled data acquisition system through a 3-m long cable. White-light reflectance spectra (450 to 720 nm) and fluorescence emissions (600 to

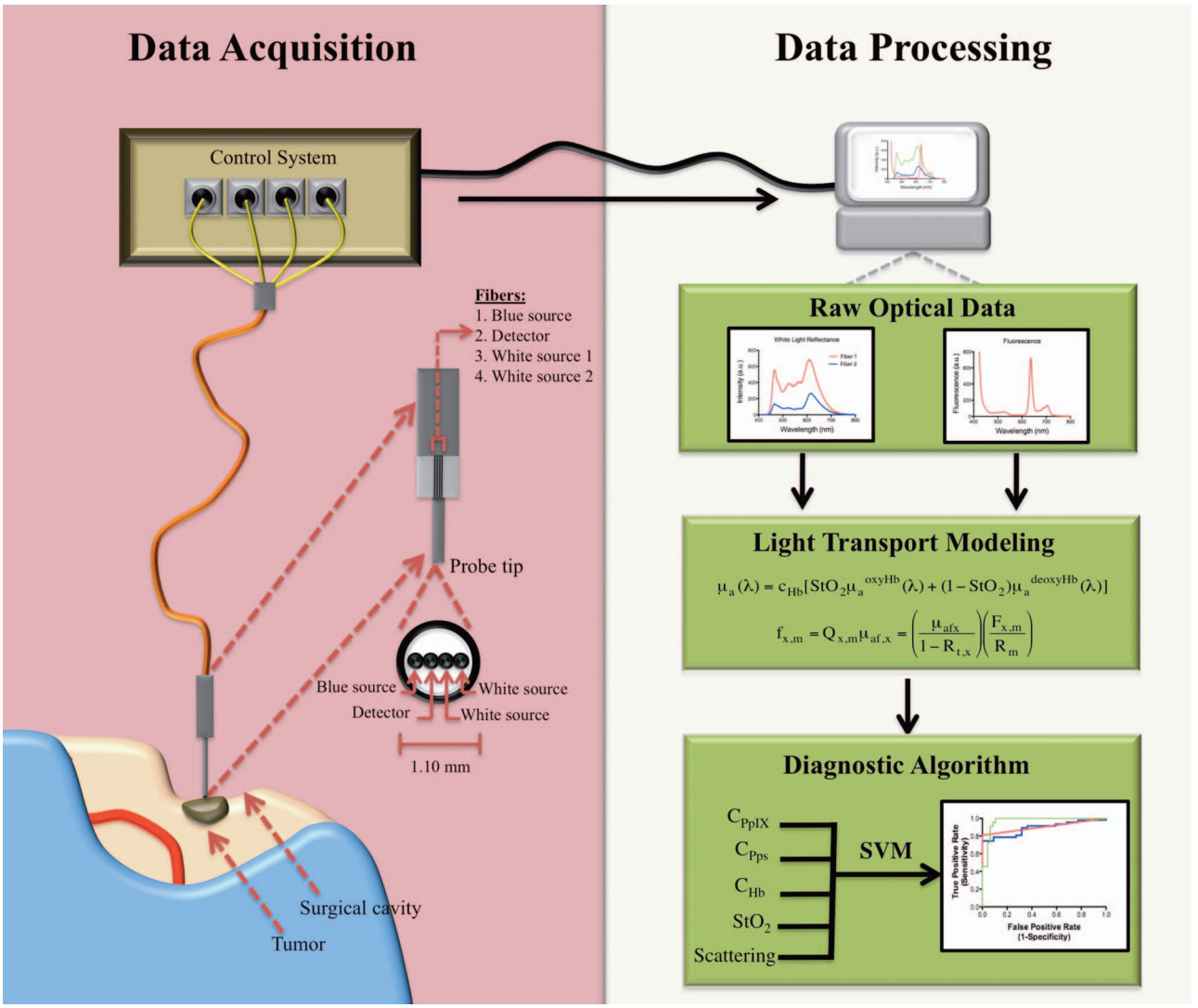

Fig. 1 Conceptual diagram of the probe measurements and data analysis. Data Acquisition (left): The intraoperative fiber optic probe with a tip diameter of ~1.1 mm is gently placed on the clean tissue surface. Sequential interrogation with white and blue light allows collection of diffuse reflectance and fluorescence spectra using a spectrometer (<0.5 s). Data Analysis: White-light reflectance data are input to a spectrally-constrained optical model to calculate the tissue optical absorption and scattering at each wavelength. These are used to correct the measured fluorescence spectrum for variations in tissue optical properties and to generate the quantitative fluorescence spectrum from which the fluorophore concentrations can be calculated (~1 s). The calculated biomarker values (e.g., c_{PpIX}, c_{Pps}, and c_{Hb}) are used in a SVM-based diagnostic algorithm to classify interrogated regions as normal tissue or tumor.

720 nm) following 405 nm excitation light were sequentially collected during each measurement. As described in detail in Kim et al.,[19,20] two white-light spectra, corresponding to different source-detector separations, are used to improve the accuracy of the tissue absorption and scattering spectra obtained from a light-transport model[19,20] (Fig. 1).

2.3.2 *Light-transport modeling*

Light-transport modeling was used to estimate the tissue optical absorption and elastic scattering properties from the white-light diffuse reflectance spectra. Optical characterization is achieved assuming that light propagation in tissue is described by the diffusion equation for boundary conditions consistent with a semi-infinite, homogeneous, optically-turbid medium.[19] Tissue can then be characterized by the optical properties of the absorption coefficient, $\mu_a(\lambda)$, and the reduced scattering coefficient, $\mu_s'(\lambda)$. These properties can be estimated at each wavelength from the white-light reflectance and then applied to the measured fluorescence spectra to correct for their distorting effects.[21–23] The estimation is achieved by minimizing the error between the probe measurements and a spectrally-constrained model of the diffuse reflectance with a Levenberg-Marquardt nonlinear curve fitting algorithm. The resulting quantitative (corrected) fluorescence spectrum was obtained from the model.

This corrected and quantitative fluorescence spectrum was then decomposed into 1. PpIX, 2. photoproducts that are generated during intraoperative exposure of PpIX to the operating lights,[24] and 3. the tissue autofluorescence due to endogenous molecules. The PpIX concentration at the tissue measurement point was calculated from the "corrected" PpIX spectrum using the known fluorescence spectrum of PpIX at unit concentration.[19]

The derived absorption and scattering spectra were analyzed to extract the intrinsic optical biomarker values. The absorption

spectra can be represented by

$$\mu_a(\lambda) = c_{Hb}[S_t O_2 \mu_a(\lambda)^{oxyHb} + (1 - S_t O_2)\mu_a(\lambda)^{deoxyHb}], \quad (1)$$

where $\mu_a(\lambda)^{oxyHb}$ and $\mu_a(\lambda)^{deoxyHb}$ are the wavelength-dependent absorption (extinction) coefficients of oxy- and deoxy-hemoglobin at concentrations of 1 g/mL, c_{Hb} represents the total hemoglobin concentration, and StO_2 is the oxygen saturation fraction (the ratio of oxyhemoglobin to total hemoglobin concentration).

The reduced scattering coefficient of tissue is represented by a wavelength-dependent power law,

$$\mu_s'(\lambda) = S_A \lambda^{-S_p}, \quad (2)$$

where S_A is the scattering amplitude and S_P is the scattering power. A forward model of diffuse reflectance and the *a priori* absorption and scattering spectra are combined, and a Levenberg-Marquardt nonlinear curve fitting algorithm is used to extract the free parameters: total hemoglobin concentration, oxygen saturation, scattering amplitude, and scattering power (Fig. 1). Further details on the algorithm can be found in Kim et al.[19]

2.4 *Neuropathological Assessment*

Histopathological analysis was performed by an experienced neuropathologist (B. T. Harris) on each biopsy specimen. Formalin-fixed, paraffin-embedded tissues were processed for hematoxylin and eosin (H&E) staining. Each H&E section was assessed for the presence of tumor cells, necrosis, and reactive astrocytosis. Tissue samples were classified as normal or abnormal (tumor) based on World Health Organization (WHO) histopathological criteria.[25] Biopsy specimens were categorized as either normal tissue, low-grade glioma (WHO grade I or II), high-grade glioma (WHO grade III or IV), or RCG. The recurrent glioma category consisted of patients who had previously undergone treatment (e.g., surgery, chemotherapy, and/or radiation) and presented tumor recurrence at the time of their second surgery. A fifth diagnostic category, labeled *all gliomas* (AG), was introduced to group all abnormal biopsy specimens together for comparison with normal control measurements.

2.5 *In Vivo Optical Data Analysis*

Prior to biopsy acquisition, *in vivo* optical measurements were acquired at multiple locations in the surgical cavity. The *in situ* intraoperative probe data associated with each biopsy acquisition were grouped based on the neuropathological assessment (e.g., tumor or normal) of their corresponding specimens.

The raw optical data acquired with the probe consisted of two reflectance spectra and one fluorescence spectrum. Analyses using the methods described in Sec. 2.3.2 (a combination of light transport modeling and curve fitting algorithms) allowed quantitative information to be derived from these raw spectra. Specifically, concentrations of oxygenated hemoglobin, de-oxygenated hemoglobin, and PpIX and associated decay photoproducts resulting from the interaction of the excitation light with the tissue were calculated. This molecular information was complemented with measures of the tissue autofluorescence and effective scattering properties.

For each probe measurement, the white-light reflectance spectrum for which the source-detector distance was $d = 260$ μm is labeled $R_1(\lambda)$ and for which $d = 520$ μm is labeled $R_2(\lambda)$. For each probe acquisition, a background measurement of the ambient light was acquired and systematically subtracted from the reflectance spectra as well as the raw fluorescence spectrum, $F_u(\lambda)$, in the range 450 to 720 nm. Instrument and data calibration were performed as described in detail in Kim et al.[19,20]

The model-derived optical spectra consisted of the absorption spectra, $\mu_a(\lambda)$, and reduced scattering spectra, $\mu_s'(\lambda)$, in the range 450 to 720 nm and diffuse reflectance spectra, $R_{t,x}(\lambda)$, in the range 450 to 720 nm for each interrogated site. The model-derived quantities that were analyzed included the PpIX concentration (c_{PpIX}), PpIX photoproduct concentration (c_{Pps}), total hemoglobin concentration (c_{Hb}), oxygen saturation fraction (StO_2), scattering amplitude (S_A), and scattering power (S_P).

2.6 *Data and Statistical Analyses*

Kolmogorov-Smirnov tests were used to ascertain normality of distributions. Wilcoxon-rank sum (Mann-Whitney) analyses were used to compare differences between spectral peaks and the derived biomarkers. Receiver operating characteristic (ROC) analysis was used to determine the area under the curve (AUC). This metric serves to quantify and summarize the diagnostic performance with AUC = 1.00 corresponding to perfect classification and AUC = 0.50 representing classification not significantly different from chance. The specificity, sensitivity, negative predictive value, and positive predictive value for qualitative visual fluorescence and c_{PpIX} are dependent on the chosen cut-off value and we used a standard methodology for determining the cut-off associated with optimal classification efficiency.[26] Data were processed and analyzed with MATLAB® software and its Bioinformatics Toolbox (Version 2010a, The Mathworks Inc., Natick, Massachusetts). Two-sided P-values <0.05 are considered statistically significant.

2.7 *Diagnostic Algorithm*

We developed a physiologically-relevant diagnostic algorithm composed of the five model-derived biomarkers. Previous studies of the brain have used various combinations of raw optical spectral peaks and peak ratios, wavelength-dependent average fluorescence lifetimes, and model-derived diffuse reflectance peaks as predictor variables in multivariate classification algorithms (e.g., linear discriminant analysis).[15,27–41] In this study, we chose quantitative biomarkers associated with neoplastic changes as variables and hypothesized that inclusion of multiple biomarkers, which individually show significant, albeit limited, classification potential, provides optimal detection accuracy.

To this end, a diagnostic algorithm for tissue classification was developed using support vector machines (SVM).[42–45] SVM algorithms are commonly used in general nonlinear classification problems in which predictor variables capture important characteristics of an individual data point. As summarized in Appendix A, SVM is a mathematical framework for generating relationships between data characteristics and a property of interest not previously known based on rules for classification derived from a training set of data points where the optimal parameters are determined by cross-validation (e.g., leave-one-out). The algorithm then applies the derived classification rules

to new data points of unknown class and assigns class membership.

2.7.1 *Dataset training and testing*

The dataset ($n = 264$ data points) was organized into two categories: normal (i.e., control normal brain) and abnormal (i.e., LGG, HGG, RCG) tissue. We used an SVM algorithm in a leave-one-out, cross-validation approach to classify tissue in which intraoperative probe data for one interrogated site was left out of the dataset. The algorithm derived from this training phase was subsequently applied to the data point left out (testing phase), a cut-off value was calculated, and the tissue was classified. This process was repeated with each individual interrogated site being left-out to build a 2-by-2 table from which the overall classification efficiency of the multiple biomarker-based diagnostic algorithm was determined and the accuracy, specificity, sensitivity, and positive and negative predictive values were calculated.

3 Results

3.1 *Neuropathology*

Intraoperative probe data were collected on 10 patients undergoing fluorescence-guided resection: five with high-grade gliomas (HGG-glioblastoma multiforme), two with low-grade glioma (LGG-mixed oligoastrocytomas) and three with RCGs. Tissue specimens from all recurrent glioma patients displayed histopathological characteristics meeting high-grade WHO criteria. A total of 88 sites were interrogated with the probe (each in triplicate) resulting in 264 spectra acquired from 26 control and 62 tumor locations.

3.2 *In Vivo Optical Data*

3.2.1 *Raw optical data*

The median spectra and interquartile range for $R_1(\lambda)$, $R_2(\lambda)$, and $F_u(\lambda)$ was calculated for normal (i.e., controls) and tumor (i.e., LGG, HGG, RCG) tissue. Wilcoxon rank-sum analysis was used to assess differences in spectral regions for $R_1(\lambda)$, $R_2(\lambda)$, and $F_u(\lambda)$ in the range $\lambda = 450$ to 720 nm. For $R_1(\lambda)$ and $R_2(\lambda)$, the whole spectrum in the range $\lambda = 450$ to 720 nm showed statistically significant differences between normal and tumor data with the most pronounced differences observed in the region corresponding to the two major absorption peaks for hemoglobin (range $\lambda = 450$ to 580 nm) ($P < 0.00001$). For $F_u(\lambda)$, statistically significant differences occurred when $\lambda < 610$ nm and $\lambda = 650$ to 680 nm. We also performed an ROC analysis and found regions for $R_1(\lambda)$ and $R_2(\lambda)$ with the highest classification efficiency for differentiating normal tissue from tumor (AUC values were 0.70 and 0.75, respectively) resulted when $\lambda = 450$ to 580 nm. For $F_u(\lambda)$, regions with the highest classification efficiency had $\lambda < 610$ nm and $\lambda = 650$ to 680 nm (AUC values were 0.75 and 0.65, respectively) (Fig. 2).

3.2.2 *Model-derived optical spectra*

The median spectra and interquartile range for $\mu_s'(\lambda)$, $\mu_a(\lambda)$, and $R_{t,x}(\lambda)$ were calculated from normal and tumor measurements. Wilcoxon-rank sum analysis was performed to assess differences in the spectral range $\lambda = 450$ to 720 nm for $\mu_a(\lambda)$, $\mu_s'(\lambda)$, and $R_{t,x}(\lambda)$. For $\mu_a(\lambda)$, a highly statistically significant difference ($P < 0.00001$) occurred in the range $\lambda = 450$ to 720 nm, whereas $\mu_s'(\lambda)$ showed a less pronounced but still statistically significant difference ($P < 0.05$). For $R_{t,x}(\lambda)$, statistically significant differences between normal tissue and tumor resulted over the range $\lambda = 450$ to 720 nm with the most pronounced differences occurring when $\lambda = 450$ to 580 nm ($P < 0.00001$). We also performed ROC analysis and found differences in $R_{t,x}(\lambda)$ with the highest classification efficiency occurring when $\lambda = 450$ to 580 nm (AUC values of approximately 0.65). The AUC values for differences in $\mu_a(\lambda)$ were approximately 0.65 in the range $\lambda = 450$ to 580 nm with a maximum of approximately 0.75 for $\lambda = 600$ to 720 nm (Fig. 3). The AUC values for the differences in $\mu_s'(\lambda)$ were approximately 0.60 over the full spectrum.

3.2.3 *Model-derived optical biomarkers*

The median value and interquartile range for c_{PpIX}, c_{Pps}, c_{Hb}, StO_2, S_A, and S_P were calculated for normal tissue and tumor and Wilcoxon-rank sum analysis was performed to assess their differences. Statistically significant increases occurred in c_{PpIX}, ($P < 0.0001$), c_{Pps} ($P < 0.0001$), c_{Hb} ($P < 0.01$), and S_P ($P < 0.0001$) in tumor compared to normal tissues, and a statistically significant decrease ($P < 0.0001$) resulted in StO_2. No significant difference was observed in S_A ($P = 0.2049$) (Fig. 4). Hence, we chose to include c_{PpIX}, c_{Pps}, c_{Hb}, StO_2, and S_P as predictor variables in the diagnostic algorithm.

3.3 *Diagnostic Algorithm Classification*

We developed an SVM diagnostic algorithm based on multiple biomarkers, which was trained and tested on $n = 264$ data points (i.e., three spectra for each interrogated site) using leave-one-out cross-validation; these results included 78 control and 186 glioma recordings (Fig. 4). We compared the diagnostic performance of this multiple biomarker algorithm to the qualitative visual assessment of fluorescence intraoperatively obtained and the quantitative measurement of PpIX concentration alone. Table 1 contains a summary of the AUCs for all gliomas as well as the low-grade, high-grade, and recurrent glioma categories for the three approaches. The optimal classification efficiency for qualitative visual fluorescence was 64% (specificity = 96%, sensitivity = 50%, positive predictive value = 97%, and negative predictive value = 45%) and for the quantitative c_{PpIX} data was 83% (specificity = 78%, sensitivity = 84%, positive predictive value = 90%, and negative predictive value = 68%) compared to 94% for the multiple biomarker algorithm (specificity = 94%, sensitivity = 94%, positive predictive value = 97%, and negative predictive value = 87%) (Table 2).

Further, we performed ROC analysis to compare the diagnostic performance of qualitative visual imaging, c_{PpIX}, and our multiple biomarker strategy. The classification algorithm was significantly more accurate with AUC = 0.94 (0.02) than qualitative visual assessment of fluorescence with AUC = 0.72(0.03) ($P < 0.00001$), and than our previously reported c_{PpIX} biomarker-only approach with AUC = 0.87(0.03) (P = 0.0055). In this study, the cut-off value with the best discrimination for c_{PpIX} was chosen as the point on the curve closest to the upper left corner of the ROC graph following standard practice and as previously reported in Valdes et al.[7] A different cut-off value (e.g., higher c_{PpIX}) could be chosen with concomitant changes in (e.g.,

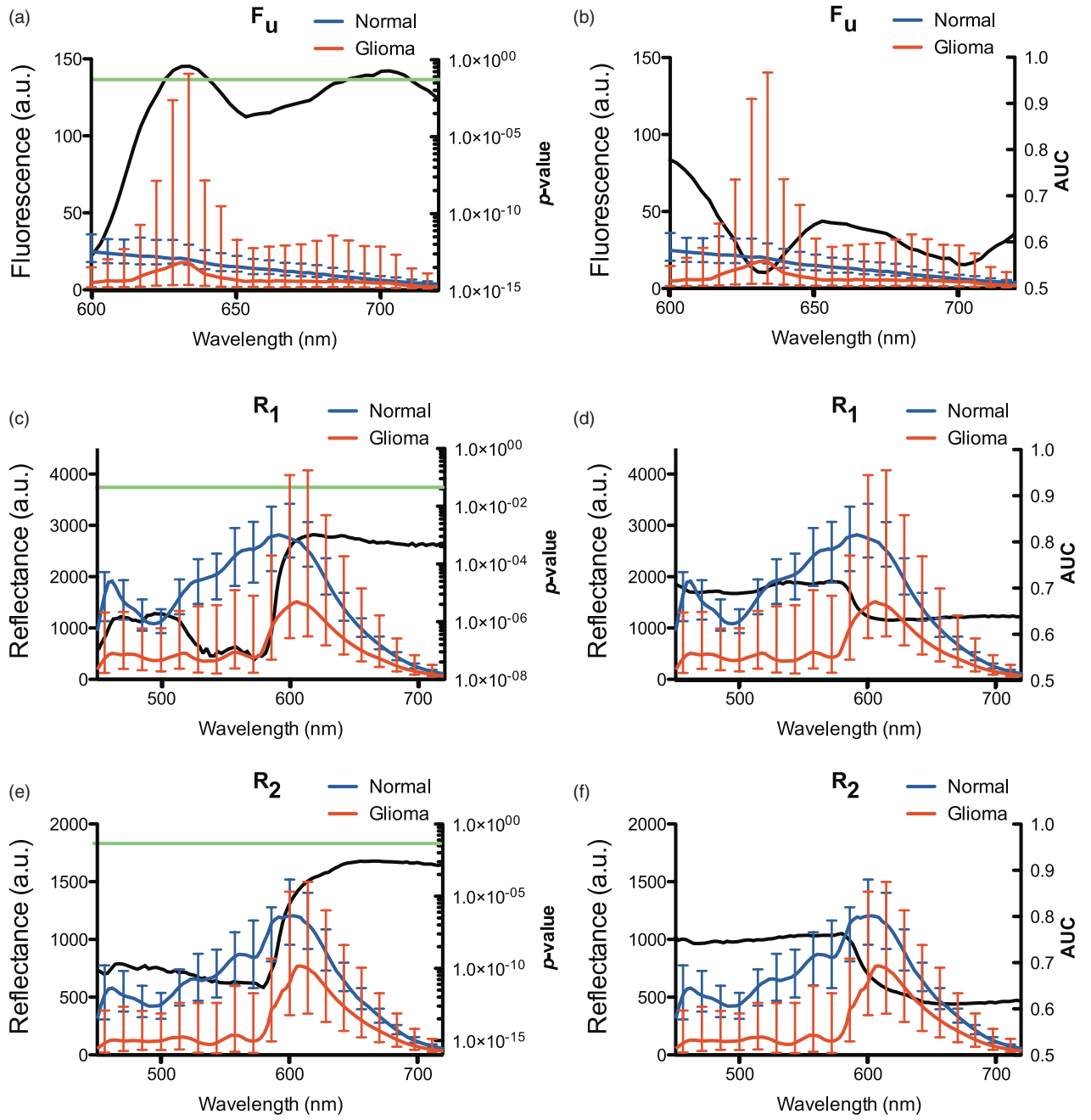

Fig. 2 Raw fluorescence and reflectance spectra. The median spectra for each of $F_u(\lambda)$ (A,B), $R_1(\lambda)$ (C,D), and $R_2(\lambda)$ (E,F) were calculated for normal (blue line) and tumor (red line) tissue. Error bars represent the interquartile range. *P*-values from the Wilcoxon-rank sum analysis are indicated by the black line, left column, with the green horizontal line crossing at $P = 0.05$. Associated AUC values are shown as the black line, right column. (Color online only.)

decreasing) sensitivity and (e.g., increasing) specificity. Table 2 summarizes the diagnostic performance of the three approaches in terms of these quantities.

4 Discussion

4.1 *Optical Strategies for Brain Tumor Surgery*

Wide-field qualitative visual fluorescence,[4,10,12,13,46–52] semi-quantitative fluorescence and/or white-light spectral characteristics,[15,27–41] and quantitative chromophore/fluorophore concentrations and/or tissue optical properties are under investigation as tools and/or data for providing intraoperative guidance during brian tumor resection procedures.[7,53] The most common and well-developed approach incorporates wide-field imaging to visualize PpIX fluorescence during the resection of high-grade gliomas. Exogenous administration of ALA leads to selective accumulation of PpIX. Blue-light excitation followed by collection of the red fluorescence emissions visible to the surgeon is used to guide resection decisions.[10,12,13,53]

Most studies of tissue discrimination through spectral characteristics have used "raw" fluorescence (endogenous or exogenously-induced) and/or white-light reflectance spectra corrected for instrument response. Various research groups have

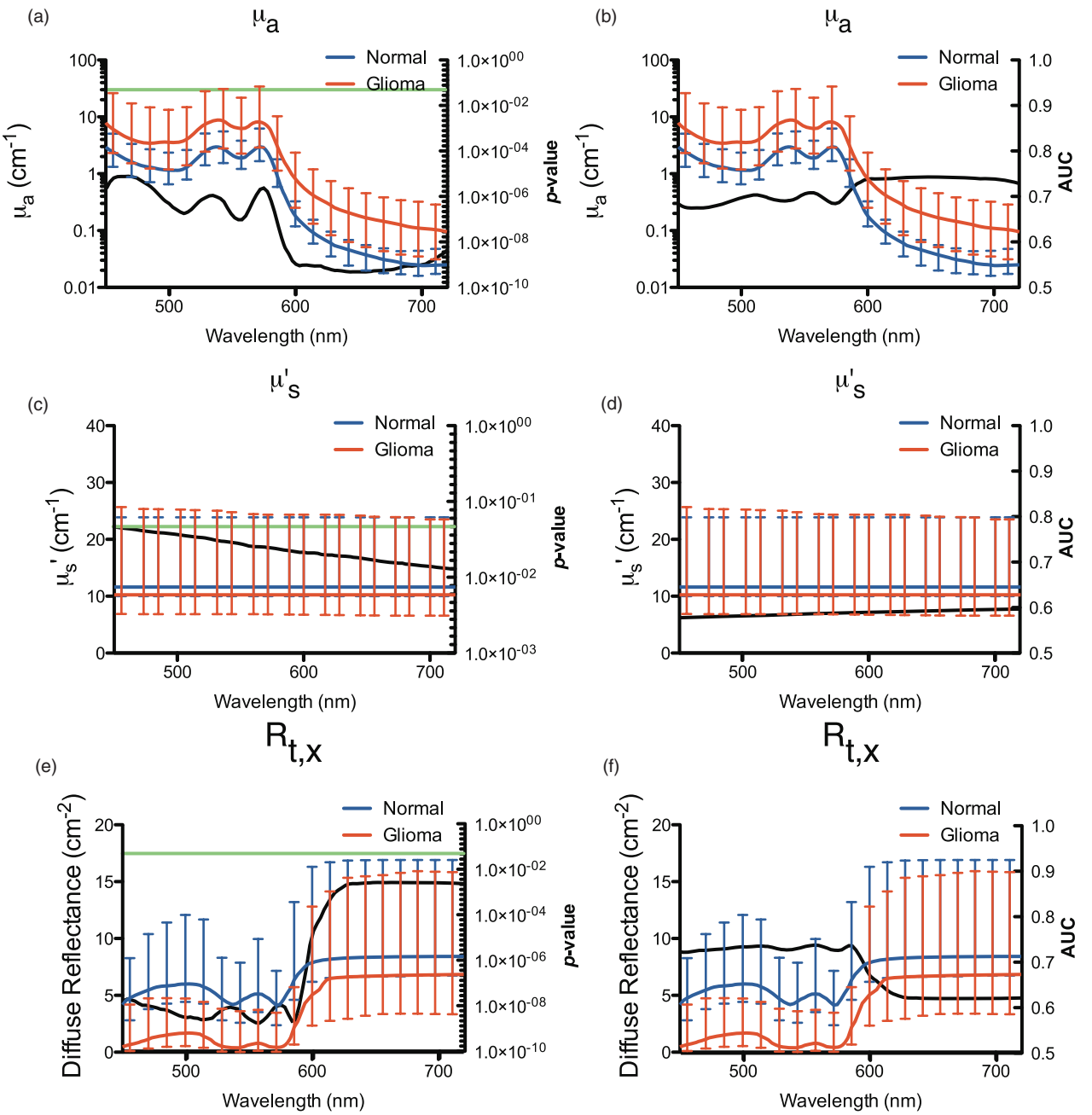

Fig. 3 Model-derived spectra. The median spectra for each of $\mu_a(\lambda)$ (A,B), $\mu_s'(\lambda)$ (C,D), and $R_{t,x}(\lambda)$ (E,F) were calculated for normal tissue (blue line) and tumor (red line). Error bars represent the interquartile range. *P*-values from the Wilcoxon-rank sum analysis are indicated by the black line, left column, with the green horizontal line crossing at $P = 0.05$. Associated AUC values are shown as the black line, right column. (Color online only.)

evaluated single spectral peaks and/or peak ratios, or combinations of spectral features for tissue identification (e.g., linear discriminant analysis).[15,27–31,33,40] For example, Marcu and colleagues[32,34,35,54] considered fluorescence peaks, peak ratios, and fluorescence lifetime values by themselves or in a linear discriminant classification algorithm. Yaroslavsky et al. estimated the tissue optical properties in brain and relationships between tissue types and distinctive features in their optical spectra.[55] Another group used white-light reflectance to calculate the total model-diffuse reflectance and assessed the diagnostic value of model-derived spectral peaks.[30]

Quantification of PpIX concentrations *in vivo* has also been used for tissue discrimination.[7,19] In this work, white-light reflectance spectra acquired *in vivo* are applied in a spectrally-constrained light-transport model to calculate tissue optical properties (i.e., μ_a, μ_s'). The measured fluorescence emission is then corrected for the distorting effects of tissue optical attenuation, so that the absolute concentrations can be calculated. Our preliminary results with this approach showed significant diagnostic improvement compared to quantitative visual fluorescence in the detection of a range of intracranial tumor histologies.

Here, we assessed the diagnostic value of visible fluorescence, raw optical data, model-derived optical spectra, and model-derived quantitative biomarkers. We hypothesized that the combination of multiple optical biomarkers quantitatively

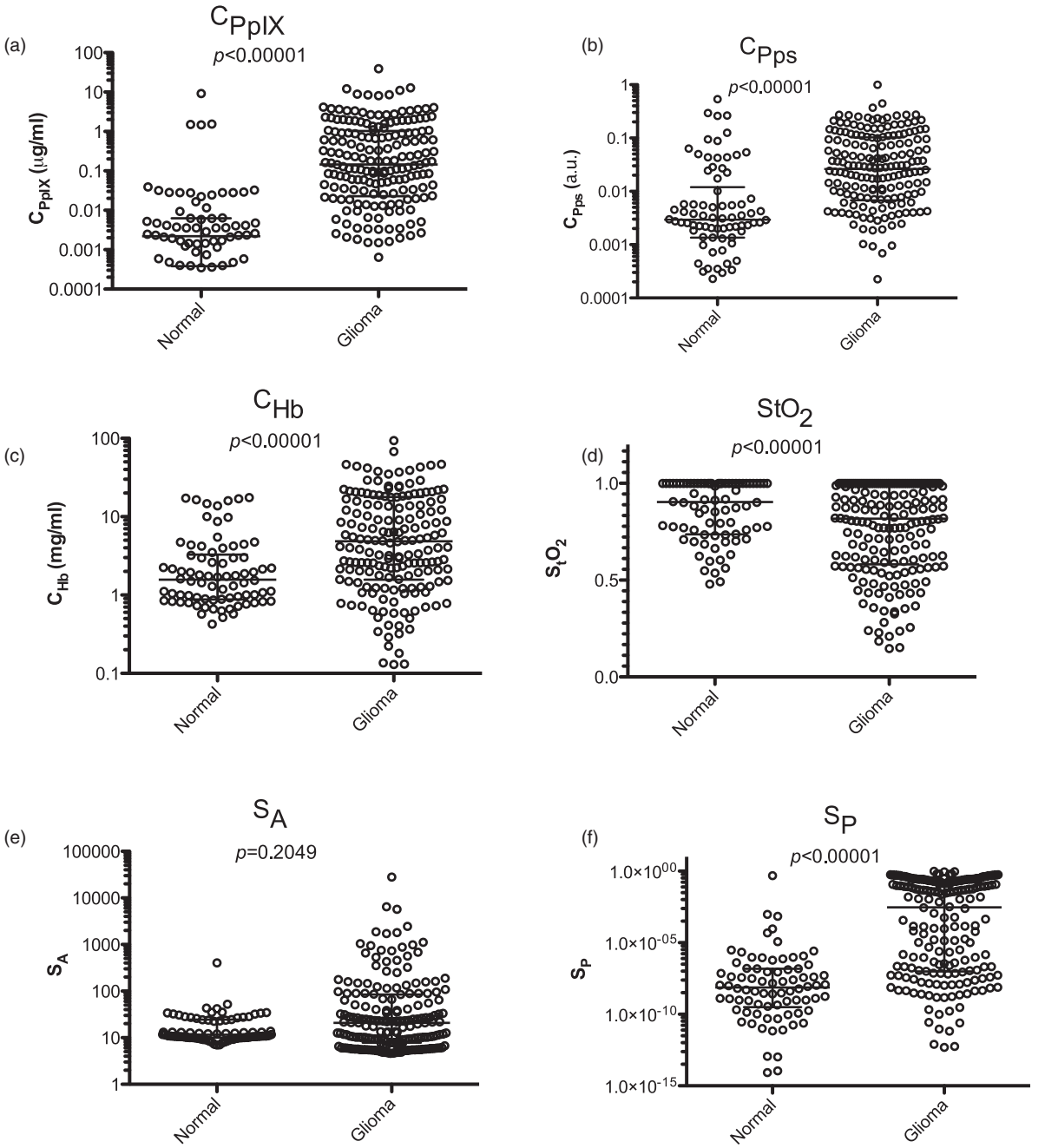

Fig. 4 Model-derived optical biomarkers. The median value for each of (A) c_{PpIX}, (B) c_{Pps}, (C) c_{Hb}, (D) StO_2, (E) S_A, and (F) S_P was calculated for normal tissue and tumor. Error bars represent the interquartile range. A significant increase in c_{PpIX}, c_{Pps}, c_{Hb}, and S_P as well as a significant decrease in StO_2 was observed for tumor compared to normal tissue. No significant change was observed for S_A.

expressed as chromophore/fluorophore concentrations and scattering parameters, which individually are indicative of neoplastic processes, is likely to offer the most diagnostic potential for brain tissue discrimination during surgery. In previous work, we found that qualitative visual assessment of ALA-induced PpIX fluorescence[4,7,12,18] provides real-time intraoperative tissue identification that does not interfere with surgical work-flow. However, the requirement for high levels of PpIX accumulation to achieve adequate signal and significant contrast for tumor discrimination with current clinical systems is a limitation that leads to low detection sensitivity even in high-grade gliomas (the tumor type where this technology is considered to be most useful).

4.2 *Raw Optical Data*

We assessed raw optical data (fluorescence and white-light reflectance) for spectrally-based tissue discrimination. We found that straightforward spectral intensity determinations were significantly different between normal tissue and tumor at various wavelengths and over wavelength regions (Fig. 2). Interestingly, the fluorescence spectra did not show significant differences at the two emission maxima of PpIX (635 and 710 nm). We

Table 1 Summary of ROC metrics. ROC analysis of three diagnostic tests. Vis = qualitative visual imaging; the standard error is in parenthesis.

	Vis	**c_{PpIX}**	**SVM**
	AUC	AUC	AUC
Group	(s.e.)	(s.e.)	(s.e.)
AG	0.72	0.87	0.94
	(0.02)	(0.03)	(0.02)
LGG	0.54	0.68	0.97
	(0.02)	(0.07)	(0.02)
HGG	0.71	0.89	0.91
	(0.03)	(0.03)	(0.02)
RCG	0.89	0.98	0.99
	(0.03)	(0.02)	(0.01)

observed significant changes in the full range of the reflectance spectra with the most pronounced differences occurring in the region of maximum hemoglobin absorption ($\lambda = \sim$450 to 580 nm). ROC analyses of the raw optical data revealed diagnostic spectral signatures with maximum AUCs of approximately 0.75 for reflectance. Fluorescence for $\lambda < 610$ nm and in the range $\lambda = 650$ to 680 nm revealed maximum AUC values of approximately 0.75 and 0.65, respectively. In contrast to previous studies,[36–39] we did not undertake an exhaustive search of peak ratios to ascertain an optimal diagnostic variable, e.g., fluorescence peak ratios; neither did we develop a multivariate algorithm using intensity peaks or peak ratios, since both strategies are already reported in the literature. These methods are independent of the assumptions underpinning the model-derived quantities and rely on absolute fluorophore/chromophore differences between normal tissue and tumor and their impact on the recorded optical spectra. Fluorescence ratios of this type have shown promise for tissue diagnostics.[15] In addition, work by Lin et al. has evaluated autofluorescence below 600 nm for tissue classification during brain tumor resection.[29,31] However, the parameters used for discriminaiton are not directly linked with pathophysiological changes,[56] which makes their biological interpretation and significance less certain.

4.3 *Model-Derived Optical Spectra*

We assessed the diagnostic potential of model-derived optical spectra for absorption, scattering, and total diffuse reflectance. The trends were similar to those reported in the literature.[31,55,57] The absorption spectrum in the range $\lambda = \sim$450 to 580 nm was dominated by hemoglobin with characteristic HbO_2 peaks at ~540 and 580 nm. In the range $\lambda = 600$ to 720 nm (a subsection of the therapeutic window investigated in this study), absorption was significantly decreased due to low hemoglobin and water absorption. Reduced scattering spectra showed the inverse relationship between wavelength and scattering predicted by the Rayleigh limit of Mie scattering.[37,57,58] The shape of the diffuse reflectance spectra showed a strong dependence on the absorption spectrum, whereas the magnitude appeared to be influenced by both scattering and absorption.[57]

Table 2 Diagnostic performance summary for biomarker-based diagnostic algorithm. Performance summary of three diagnostic tests. Vis = qualitative visual imaging; Classification efficiencies, sensitivities (Sn), negative predictive values (NPV), specificities (Sp), and positive predictive values (PPV) for tumor tissue diagnosis are tabulated.

	Classification efficiency(%)	Sn (%)	NPV (%)	Sp (%)	PPV (%)
		SVM			
AG	94	94	87	94	97
LGG	96	94	88	100	100
HGG	92	92	87	91	95
RCG	98	98	86	100	100
		c_{PpIX}			
AG	83	84	68	78	90
LGG	63	50	44	93	95
HGG	81	75	68	91	94
RCG	97	96	75	100	100
		VIS			
AG	64	50	45	96	97
LGG	35	8	31	100	100
HGG	67	50	53	95	94
RCG	80	78	33	100	100

Similar to the raw data, we found significant differences between tumor and normal tissue in the model-derived spectra for absorption, scattering, and diffuse reflectance across all wavelengths. Diffuse reflectance showed pronounced normal-tumor tissue differences ($P < 0.00001$) in the range $\lambda = \sim$450 to 580 nm, consistent with previous work on the brain,[31,55,57,59] whereas the reduced scattering showed less significant differences ($P < 0.05$). Previous studies by Lin et al.[29,31] have reported autofluorescence and diffuse reflectance spectra with varying degrees of differences between gray matter, white matter, and tumor. In this study, normal tissue spectra were mostly obtained from gray matter[29] because the majority of control measurements were acquired from gray matter cortex following durotomy but prior to the first incision. While some bias may have been introduced by the undersampling of white matter, we measured physiologically meaningful biomarkers that represent changes (e.g., angiogenesis, hypoxia, etc.) expected to be more different in tumor versus normal tissue (e.g., gray or white matter) than between normal tissues (e.g., gray and white matter). Nonetheless, further investigation of systematic differences between normal gray and white matter, and their impact on tumor spectral and biomarker identification is warranted.

For the model-derived spectra, the absorption spectrum yielded AUC values of approximately 0.65 in the region

dominated by hemoglobin absorption and maximum AUC values of approximately 0.75 in the range $\lambda = 600$ to 720 nm. Lin et al.[30] also considered the diagnostic potential of model-derived spectral peaks, specifically for diffuse reflectance, and reported AUC values of ~0.65 in the region 450 to 600 nm and ~0.75 in the region 600 to 720 nm. The small discrepancies between these results and ones we report here can most likely be attributed to differences in tumor histologies between the two studies and the small number of patients involved. Future work with larger enrollments will more closely approximate the true data distribution among brain tumors and resolve these relatively minor differences.

Model-derived optical spectra provide a theoretical framework with which to understand tissue-light interactions. In contrast to discrimination based on raw spectral data, model-derived spectral peaks/peak ratios account for how light interacts with tissue.[37] Although this strategy incorporates a biophysical framework that is expected to enhance the information contained in the raw spectral data, it still depends on the choice of spectral data (even following optimization) and usually requires many variables to be extracted from the spectra for tissue classification. It also requires adequate model-data fitting for valid predictions that are based on spectral changes that are indirectly related to specific pathophysiological processes, and therefore, could limit clinical interpretation and acceptance.

4.4 *Quantitative Optical Biomarkers*

Gliomas are a heterogeneous group of tumors ranging from well-circumscribed WHO grade I lesions, with minimal histological de-differentiation, to the highly invasive and malignant WHO grade IV, glioblastoma multiforme, with high intra-tumoral heterogeneity, necrosis, endothelial proliferation, and genetic atypia. Conventional histopathological diagnosis of gliomas requires a multifaceted assessment of tissue changes (e.g., nuclear abnormality, endothelial proliferation, necrosis, and increased cell density), and since they are genetically diverse with complex expression profiles, combinations of biomarkers are likely to more accurately delineate these tumors.[60]

Toward this end, we examined quantitative values of five optical biomarker groups to develop a diagnostic algorithm for intraoperative tissue classification: 1. PpIX concentration, 2. PpIX photoproduct concentration, 3. total hemoglobin concentration, 4. oxygen saturation fraction, and 5. scattering parameters (S_A and S_P). PpIX has been shown to selectively accumulate in brain tumors following exogenous administration of ALA. Neoplastic changes include up- and/or down-regulated protein expression (e.g., ferrochelatase), dysregulated substrate uptake mechanisms, microenvironmental changes, abnormal metabolism, increased proliferative potential, and compromised blood-brain barrier.[4,61] We recently found a significant improvement in tumor detection, including increased sensitivity in low-grade gliomas (although at a lower level than in high-grade tumor) when c_{PpIX} is quantified (relative to visual assessment).[7] These results demonstrate that quantitative evaluation of c_{PpIX} (and associated photoproducts, i.e., c_{Pps}) holds promise as an intraoperative biomarker for guiding surgical resection (Fig. 4). While photobleaching may occur (and be variable) in the operating room, which could distort the c_{PpIX} readings (and their correspondence with tumor), neurosurgical resection is dynamic (i.e., exposure times to newly presented tumor are typically short) and we have not observed evidence of these potentiallty deleterious effects having altered the diagnostic signature of c_{PpIX} in malignant versus normal tissues. Presumably, c_{Pps} originates from ALA-induced PpIX conversion (which is selectively enhanced in tumors) and its incorporation within the diagnostic discriminator may serve to balance loss of c_{PpIX} signal from photobleaching effects.

Quantitative values of StO_2 and c_{Hb} are indicators of different, but interrelated and inter-dependent biological processes. Tissue hypoxia (i.e., low levels of StO_2) is associated with malignant progression and is a consequence of multiple processes occurring in the tumor microenvironment (angiogenesis, balance of aerobic/anaerobic metabolism, cell survival, and invasion).[62] Specifically, hypoxia is an outcome of the metabolic adaptation of tumors to anaerobic growth,[5,63] i.e., survival adaptation to increased glycolysis, resulting in part from the increased metabolism and oxygen demand of rapidly proliferating cells and the decreased oxygen supply provided by the microvascular density.[64] It may also positively alter the diffuse infiltration of gliomas by increasing local acidic conditions.[65] As a result, lower StO_2 (Fig. 4) is a biological indicator (i.e., a biomarker) of tissue hypoxia associated with tumorigenesis.

Angiogenesis (formation of new blood vessels) occurs in tumors at increased levels in a disorganized and inefficient fashion (tortuous dead-ends, overproduction of capillary networks, etc.) and with abnormal vascular structure and performance (highly permeable and dilated vessels).[5,63,66] It is a pre-requisite for tumor formation, growth, and progression.[63] Angiogenesis is also related to hypoxia because new vessels form in tumors partly as a physiological response to lack of oxygen.[62,64,65,67] Regions of increased vasculature have increased levels of blood elevating c_{Hb} and making it an indicator of tumor angiogenesis (Fig. 4).

Tumors undergo morphological changes at the tissue, cellular, and sub-cellular levels. Changes in nuclear size and shape, organelle content, and morphology occur at the cellular and sub-cellular scales, whereas increased cellular density,, and disorganized tissue networks and vasculature occur at the tissue level. Elastic scattering of light in tissue reflects the size and shape of scatterers, which can be related to these underlying sub-cellular, cellular, and tissue characteristics.[37,58,68,69] Here, we used a wavelength-dependent power law $\mu_s' = S_A\lambda^{-S_P}$ to model the reduced scattering spectrum, $\mu_s'(\lambda)$, yielding quantitative scattering parameters, S_A and S_P, corresponding to the scattering amplitude and power of tissue. Scattering parameters serve as biomarkers of morphological changes that occur in tumors, typically being increased by the inhomogeneities that exist[58] (Fig. 4).

These quantitative biomarkers serve as indicators of important biological processes (e.g., angiogenesis, hypoxia) occurring in gliomas. Given the inter- and intra-tumor heterogeneity of gliomas and the multifaceted character of the neoplastic processes involved, intraoperative tumor (Table 1) identification is likely to benefit from the evaluation of multiple factors (i.e., biomarkers).

4.5 *Diagnostic Algorithm*

We developed an SVM algorithm, commonly applied in general, nonlinear problems,[42–44] to incorporate the individual

predictive and diagnostic contributions from the five model-derived quantitative biomarkers (i.e., c_{PpIX}, c_{Pps}, c_{Hb}, StO_2, and S_P) for tissue classification. We found superior diagnostic performance resulted from this multiple biomarker-based strategy [classification efficiency = 94%; ROC AUC = 0.94(0.02)] relative to raw spectroscopic fluorescence, model-derived spectra, and intraoperative visual fluorescence [classification efficiency = 64%; ROC AUC = 0.72(0.02)].

ALA-induced PpIX fluorescence as visualized with a state-of-the-art surgical microscope showed a diagnostic performance in LGG that is marginally greater than chance [AUC of 0.54(0.02)]. As expected, visible fluorescence in HGG performs significantly better with an AUC of 0.71(0.03). With c_{PpIX} as a single biomarker, the AUC for HGG increases to 0.89(0.03) and also improves to 0.68(0.07) for LGG. Interestingly, the diagnostic performance in LGG with c_{PpIX} is comparable to qualitative visual fluorescence in HGG, but does not achieve the performance attained with c_{PpIX}. Multiple quantitative biomarkers offer significantly improved diagnostic performance ($P < 0.00001$), especially in LGG [to 0.97(0.02) from 0.54(0.02) using visible fluorescence and 0.68(0.07) using c_{PpIX} alone]. These encouraging results suggest that multiple quantitative biomarkers may be able to detect both tumor bulk and infiltrating margins, especially in low-grade gliomas where the impact on patient prognosis and survival could be substantial.

While these data are promising, the results were generated from a nonrandomized study with a limited number of patients. Nonetheless, as a proof-of-concept, the strategy does significantly improve tumor detection, although further validation of its predictive power in a larger cohort of gliomas is still required. However, the balance between sensitivity and specificity may be surgeon and even case-specific, since concerns for patient safety and/or the risk of functional impairment secondary to surgery often independently override the resection decision of whether tumor remains in the operative field. From this perspective, the comparative analysis of diagnostic performance presented here is somewhat simplistic, and a robust diagnostic algorithm that the surgeon could adjust for (or even during) a case to emphasize sensitivity or specificity might be more attractive, since the probability of tumor is only one factor weighed in the decision to resect any given portion of brain tissue. In practice, intraoperative probe-based sampling of brain tissue is likely to be of modest value to the surgeon because of its limited capacity to efficiently interrogate the surgical field. Hence, discrimination algorithms of the type described here will not have much impact in the operating room (OR) unless wide-field imaging technology is developed, which can recover the quantitative optical biomarkers that have been used.

5 Conclusions

Based on retrospective data collected in 10 glioma patients, intraoperative identification of tumor is significantly improved when multiple optical biomarkers are quantified and incorporated into a diagnostic algorithm based on support vector machine classification relative to qualitative visual fluorescence or characteristics obtained from raw optical spectra or model-derived spectral features. Prospective validation of the predictive power of the algorithm in a larger cohort of patients remains to be completed and even the diagnostic training of the approach may benefit from additional data collected from a broader number of tumors meeting the low and high grade WHO histopathological criteria. While the quantification of chromophore/fluorophore concentrations and scattering parameters opens the door to the inclusion of multiple biomarkers representing processes characteristic of tumor biology in an algorithm that extends diagnostic performance beyond traditional single biomarker (e.g., PpIX), single modality (e.g., fluorescence) or "black box" spectral techniques, clinical utility of the method will necessitate the development of an equivalent wide-field approach.

Acknowledgments

This work was supported in part by National Institutes of Health Grant No. R01NS052274-01A2 (D. W. Roberts) and award K25 CA138578 (F. Leblond). Carl Zeiss (Carl Zeiss Surgical GmbH, Oberkochen, Germany) and Medtronic Navigation (Medtronic, Louisville, Colorado) provided the fluorescence-enabled OPMI Pentero® operating microscope and StealthStation® Treon® navigation system, respectively. DUSA Pharmaceuticals (DUSA Pharmaceuticals, Tarrytown, New York) supplied the ALA. Drs. Kim and Wilson have a provisional patent (61,297,969) for the intraoperative probe used in this study.

Appendix A

An SVM classification algorithm finds the optimal (unique) separating hyperplane (OSH) between two classes by maximizing the margin, δ, in feature space between the closest point(s) of both classes. Individual data points (e.g., an interrogated tissue site) are known as objects and are composed of a set of predictor variables or attributes (i.e., the parameters used to describe the individual data points, such as c_{PpIX}, c_{Hb} in this work). An object, x, has n attributes (i.e., coordinates) in input space, R^I, such that $x_i = (x_1, x_2, \ldots x_n)$, where x_j is a real number, $x_j \in R$ for $j = 1, 2, \ldots, n$. Each object belongs to a given class $y_i \in \{-1, 1\}$. SVM then maps objects from the original input space on to a higher dimensional feature space using nonlinear functions known as feature functions.[42,44,45,70]

We consider a training set, T, of m objects and their classes, $T = \{(\mathbf{x}_1, y_1), (\mathbf{x}_2, y_2), \ldots, (\mathbf{x}_m, y_m), \}$. A set of features functions, $\phi_1, \phi_2, \ldots, \phi_h$, is defined that map any object $\mathbf{x}$ into vector $\boldsymbol{\phi}(\mathbf{x})$:

$$\mathbf{x} = (x_1, x_2, \ldots, x_n) \rightarrow \boldsymbol{\phi}(\mathbf{x}) = (\phi_1(\mathbf{x}), \phi_2(\mathbf{x}), \ldots, \phi_h(\mathbf{x}))\,. \tag{9}$$

After mapping, we form a set of objects in feature space, R^F, based on their individual class assignments:

$$\Phi(T) = [\phi(\mathbf{x}_1, y_1), \phi(\mathbf{x}_2, y_2), \ldots, \phi(\mathbf{x}_m, y_m)]\,. \tag{10}$$

The training set in feature space (i.e., $\phi(T)$) can be linearly classified if the appropriate feature functions (i.e., $\boldsymbol{\phi}(\mathbf{x})$) are used. Transformed attributes are known as features, and a vector is the set of features that make up an object. vectors that constrain the margin width are known as support vectors.[42,44,45,70] in feature space, objects can be separated by class with associated error costs when no perfect classification is achievable, which becomes a constrained-optimization problem (i.e., to find the OSH minimization of a quadratic function under linear constraints) that can be solved by a Lagrangian transformation, which

generalizes the problem to both linear and nonlinear SVM models. Here, we used a sequential minimal optimization algorithm to solve the optimization problem. In a nonlinear SVM, the objects' class (i.e., $\mathbf{x}_k$) is given by

$$class(\mathbf{x}_k) = sign\,[w \cdot \phi(\mathbf{x}_k) + b] = sign\left[\sum_{i=1}^{m} \lambda_i y_i \phi(\mathbf{x}_i) \cdot \phi(\mathbf{x}_k)\right], \quad (11)$$

where $\Lambda = (\lambda_1, \lambda_2, \ldots, \lambda_m)$ is the set of Lagrange multipliers from the training objects $\mathbf{x} = (x_1, x_2, \ldots, x_m)$. Under certain conditions (Mercer's conditions), an inner product in feature space has an equivalent kernel in input space. In this case, simple nonlinear kernel functions can be used to compute $\phi(\mathbf{x}_i) \cdot \phi(\mathbf{x}_k)$ and perform the nonlinear mapping of feature functions, such that

$$K(\mathbf{X}_i, \mathbf{X}_j) = \phi(\mathbf{X}_i) \cdot \phi(\mathbf{X}_j). \quad (12)$$

The training objects with $\lambda_i > 0$ represent the support vectors. The objects with $\lambda_i = 0$ are not important in the SVM model, and all that is needed to classify objects are the support vectors and $\lambda_i > 0$.[42,45,70]

We optimized SVM parameters (e.g., kernels functions) and applied the commonly used Gaussian radial basis function for classification,

$$K(\mathbf{X}_i, \mathbf{X}_j) = \phi(\mathbf{X}_i) \cdot \phi(\mathbf{X}_j) = e^{-\frac{\|x-y\|^2}{2\sigma^2}}, \quad (13)$$

where σ controls the shape of the separating hyperplane. Kernel function parameter optimization for σ and the soft margin constraint occurred by performing a grid search from 0.05 to 10 for σ and from 1 to 200 for the soft margin constraint to find the highest classification efficiency.[45] We optimized the SVM classification algorithm parameters with a value of $\sigma = 0.2$, a soft margin penalty error of 81 (to provide a balance between complexity, over-fitting, and tolerance of the diagnostic algorithm for misclassification) and an average of 179 support vectors.[45]

References

1. L. M. DeAngelis, "Brain tumors," *N. Engl. J. Med.* **344**(2), 114–123 (2001).
2. M. Jansen, S. Yip, and D. N. Louis, "Molecular pathology in adult gliomas: diagnostic, prognostic, and predictive markers," *Lancet Neurol.* **9**(7), 717–726 (2010).
3. M. Lacroix, D. Abi-Said, D. R. Fourney, Z. L. Gokaslan, W. Shi, F. DeMonte, F. F. Lang, I. E. McCutcheon, S. J. Hassenbusch, E. Holland, K. Hess, C. Michael, D. Miller, and R. Sawaya, "A multivariate analysis of 416 patients with glioblastoma multiforme: prognosis, extent of resection, and survival," *J. Neurosurg.* **95**(2), 190–198 (2001).
4. B. W. Pogue, S. Gibbs-Strauss, P. A. Valdes, K. Samkoe, D. W. Roberts, and K. D. Paulsen, "Review of neurosurgical fluorescence imaging methodologies," *IEEE J. Sel. Top. Quantum Electron.* **16**(3), 493–505 (2010).
5. E. G. Van Meir, C. G. Hadjipanayis, A. D. Norden, H. K. Shu, P. Y. Wen and J. J. Olson, "Exciting new advances in neuro-oncology: the avenue to a cure for malignant glioma," *Ca-Cancer J. Clin.* **60**(3), 166–193 (2010).
6. F. W. Floeth and W. Stummer, "The value of metabolic imaging in diagnosis and resection of cerebral gliomas," *Nat. Clin. Pract. Neurol.* **1**(2), 62–63 (2005).
7. P. A. Valdes, F. Leblond, A. Kim, B. T. Harris, B. C. Wilson, X. Fan, T. D. Tosteson, A. Hartov, S. Ji, K. Erkmen, N. E. Simmons, K. D. Paulsen, and D. W. Roberts, "Quantitative fluorescence in intracranial tumor: implications for ALA-induced PpIX as an intraoperative biomarker," *J. Neurosurg.* **115**(1), 11–17 (2011).
8. F. K. Albert, M. Forsting, K. Sartor, H. P. Adams, and S. Kunze, "Early postoperative magnetic resonance imaging after resection of malignant glioma: objective evaluation of residual tumor and its influence on regrowth and prognosis," *Neurosurgery* **34**(1), 45–60; discussion 60–41 (1994).
9. M. J. McGirt, K. L. Chaichana, M. Gathinji, F. J. Attenello, K. Than, A. Olivi, J. D. Weingart, H. Brem, and A. R. Quinones-Hinojosa, "Independent association of extent of resection with survival in patients with malignant brain astrocytoma," *J. Neurosurg.* **110**(1), 156–162 (2009).
10. W. Stummer, U. Pichlmeier, T. Meinel, O. D. Wiestler, F. Zanella, and H. J. Reulen, "Fluorescence-guided surgery with 5-aminolevulinic acid for resection of malignant glioma: a randomised controlled multicentre phase III trial," *Lancet Oncol.* **7**(5), 392–401 (2006).
11. A. Johansson, G. Palte, O. Schnell, J. C. Tonn, J. Herms, and H. Stepp, "5-Aminolevulinic acid-induced protoporphyrin IX levels in tissue of human malignant brain tumors," *Photochem. Photobiol.* **86**(6), 1373–1378 (2010).
12. D. W. Roberts, P. A. Valdes, B. T. Harris, K. M. Fontaine, A. Hartov, X. Fan, S. Ji, S. S. Lollis, B. W. Pogue, F. Leblond, T. D. Tosteson, B. C. Wilson, and K. D. Paulsen, "Coregistered fluorescence-enhanced tumor resection of malignant glioma: relationships between delta-aminolevulinic acid-induced protoporphyrin IX fluorescence, magnetic resonance imaging enhancement, and neuropathological parameters," *J. Neurosurg.* **114**(3), 595–603 (2011).
13. W. Stummer, A. Novotny, H. Stepp, C. Goetz, K. Bise, and H. J. Reulen, "Fluorescence-guided resection of glioblastoma multiforme by using 5-aminolevulinic acid-induced porphyrins: a prospective study in 52 consecutive patients," *J. Neurosurg.* **93**(6), 1003–1013 (2000).
14. P. A. Valdes, A. Kim, M. Brantsch, C. Niu, Z. B. Moses, T. D. Tosteson, B. C. Wilson, K. D. Paulsen, D. W. Roberts, and B. T. Harris, "δ-aminolevulinic acid-induced protoporphyrin IX concentration correlates with histopathologic markers of malignancy in human gliomas: the need for quantitative fluorescence-guided resection to identify regions of increasing malignancy," *Neuro. Oncol.* **13**(8), 846–856 (2011).
15. J. C. Richter, N. Haj-Hosseini, S. Andersson-Engel, and K. Wardell, "Fluorescence spectroscopy measurements in ultrasonic navigated resection of malignant brain tumors," *Lasers Surg. Med.* **43**(1), 8–14 (2011).
16. R. Weissleder and M. J. Pittet, "Imaging in the era of molecular oncology," *Nature* **452**(7187), 580–589 (2008).
17. P. Y. Wen and S. Kesari, "Malignant gliomas in adults," *N. Engl. J. Med.* **359**(5), 492–507 (2008).
18. P. A. Valdes, X. Fan, S. Ji, B. T. Harris, K. D. Paulsen, and D. W. Roberts, "Estimation of brain deformation for volumetric image updating in protoporphyrin IX fluorescence-guided resection," *Stereotact. Funct. Neurosurg.* **88**(1), 1–10 (2010).
19. A. Kim, M. Khurana, Y. Moriyama, and B. C. Wilson, "Quantification of in vivo fluorescence decoupled from the effects of tissue optical properties using fiber-optic spectroscopy measurements," *J. Biomed. Opt.* **15**(6), 067006 (2010).
20. A. Kim, M. Roy, F. Dadani, and B. C. Wilson, "A fiberoptic reflectance probe with multiple source-collector separations to increase the dynamic range of derived tissue optical absorption and scattering coefficients," *Opt. Express* **18**(6), 5580–5594 (2010).
21. J. Wu, M. S. Feld, and R. P. Rava, "Analytical model for extracting intrinsic fluorescence in turbid media," *Appl. Opt.* **32**(19), 3585–3595 (1993).
22. R. Weersink, M. S. Patterson, K. Diamond, S. Silver, and N. Padgett, "Noninvasive measurement of fluorophore concentration in turbid media with a simple fluorescence /reflectance ratio technique," *Appl. Opt.* **40**(34), 6389–6395 (2001).
23. M. G. Muller, I. Georgakoudi, Q. Zhang, J. Wu, and M. S. Feld, "Intrinsic fluorescence spectroscopy in turbid media: disentangling effects of scattering and absorption," *Appl. Opt.* **40**(25), 4633–4646 (2001).
24. J. S. Dysart and M. S. Patterson, "Photobleaching kinetics, photoproduct formation, and dose estimation during ALA induced PpIX PDT of MLL cells under well oxygenated and hypoxic conditions," *Photochem. Photobiol. Sci.* **5**(1), 73–81 (2006).

25. D. N. Louis, H. Ohgaki, O. D. Wiestler, W. K. Cavenee, P. C. Burger, A. Jouvet, B. W. Scheithauer, and P. Kleihues, "The 2007 WHO classification of tumours of the central nervous system," *Acta Neuropathol.* **114**(2), 97–109 (2007).
26. D. E. Shapiro, "The interpretation of diagnostic tests," *Stat. Methods Med. Res.* **8**(2), 113–134 (1999).
27. N. Haj-Hosseini, J. Richter, S. Andersson-Engels and K. Wardell, "Optical touch pointer for fluorescence guided glioblastoma resection using 5-aminolevulinic acid," *Lasers Surg. Med.* **42**(1), 9–14 (2010).
28. R. Ishihara, Y. Katayama, T. Watanabe, A. Yoshino, T. Fukushima and K. Sakatani, "Quantitative spectroscopic analysis of 5-aminolevulinic acid-induced protoporphyrin IX fluorescence intensity in diffusely infiltrating astrocytomas," *Neurol. Med. Chir. (Tokyo)* **47**(2), 53–57; discussion 57 (2007).
29. W. C. Lin, D. I. Sandberg, S. Bhatia, M. Johnson, G. Morrison, and J. Ragheb, "Optical spectroscopy for in-vitro differentiation of pediatric neoplastic and epileptogenic brain lesions," *J. Biomed. Opt.* **14**(1), 014028 (2009).
30. W. C. Lin, D. I. Sandberg, S. Bhatia, M. Johnson, S. Oh, and J. Ragheb, "Diffuse reflectance spectroscopy for in vivo pediatric brain tumor detection," *J. Biomed. Opt.* **15**(6), 061709 (2010).
31. W. C. Lin, S. A. Toms, M. Johnson, E. D. Jansen, and A. Mahadevan-Jansen, "*In vivo* brain tumor demarcation using optical spectroscopy," *Photochem. Photobiol.* **73**(4), 396–402 (2001).
32. L. Marcu, J. A. Jo, P. V. Butte, W. H. Yong, B. K. Pikul, K. L. Black, and R. C. Thompson, "Fluorescence lifetime spectroscopy of glioblastoma multiforme," *Photochem. Photobiol.* **80**, 98–103 (2004).
33. S. K. Majumder, S. Gebhart, M. D. Johnson, R. Thompson, W. C. Lin, and A. Mahadevan-Jansen, "A probability-based spectroscopic diagnostic algorithm for simultaneous discrimination of brain tumor and tumor margins from normal brain tissue," *Appl. Spectrosc.* **61**(5), 548–557 (2007).
34. P. V. Butte, Q. Fang, J. A. Jo, W. H. Yong, B. K. Pikul, K. L. Black, and L. Marcu, "Intraoperative delineation of primary brain tumors using time-resolved fluorescence spectroscopy," *J. Biomed. Opt.* **15**(2), 027008 (2010).
35. P. V. Butte, A. N. Mamelak, M. Nuno, S. I. Bannykh, K. L. Black, and L. Marcu, "Fluorescence lifetime spectroscopy for guided therapy of brain tumors," *Neuroimage* **54S1**, S125–S135 (2011).
36. N. Ramanujam, "Fluorescence spectroscopy of neoplastic and non-neoplastic tissues," *Neoplasia* **2**(1–2), 89–117 (2000).
37. R. Richards-Kortum and E. Sevick-Muraca, "Quantitative optical spectroscopy for tissue diagnosis," *Annu. Rev. Phys. Chem.* **47**, 555–606 (1996).
38. K. Sokolov, M. Follen, and R. Richards-Kortum, "Optical spectroscopy for detection of neoplasia," *Curr. Opin. Chem. Biol.* **6**(5), 651–658 (2002).
39. S. A. Toms, P. E. Konrad, W. C. Lin, and R. J. Weil, "Neuro-oncological applications of optical spectroscopy," *Technol. Cancer Res. Treat.* **5**(3), 231–238 (2006).
40. S. A. Toms, W. C. Lin, R. J. Weil, M. D. Johnson, E. D. Jansen, and A. Mahadevan-Jansen, "Intraoperative optical spectroscopy identifies infiltrating glioma margins with high sensitivity," *Neurosurgery* **57**(4 Suppl), 382–391; discussion 382–391 (2005).
41. W. H. Yong, P. V. Butte, B. K. Pikul, J. A. Jo, Q. Fang, T. Papaioannou, K. Black, and L. Marcu, "Distinction of brain tissue, low grade and high grade glioma with time-resolved fluorescence spectroscopy," *Front Biosci.* **11**, 1255–1263 (2006).
42. C. J. C. Burges, "A tutorial on support vector machines for pattern recognition," *Data Min. Knowl. Discov.* **2**(2), 121–167 (1998).
43. R. O. Duda, P. E. Hart, and D. G. Stork, *Pattern classification*, Wiley, New York (2001).
44. W. S. Noble, "What is a support vector machine?," *Nat. Biotechnol.* **24**(12), 1565–1567 (2006).
45. R. G. Brereton and G. R. Lloyd, "Support vector machines for classification and regression," *Analyst* **135**(2), 230–267 (2010).
46. M. S. Eljamel, G. Leese and H. Moseley, "Intraoperative optical identification of pituitary adenomas," *J. Neuro-Oncol.* **92**(3), 417–421 (2009).
47. M. Hefti, G. von Campe, M. Moschopulos, A. Siegner, H. Looser, and H. Landolt, "5-aminolevulinic acid induced protoporphyrin IX fluorescence in high-grade glioma surgery: a one-year experience at a single institutuion," *Swiss Med. Wkly.* **138**(11–12), 180–185 (2008).
48. T. Kuroiwa, Y. Kajimoto, and T. Ohta, "Comparison between operative findings on malignant glioma by a fluorescein surgical microscopy and histological findings," *Neurol. Res.* **21**(1), 130–134 (1999).
49. A. Nabavi, H. Thurm, B. Zountsas, T. Pietsch, H. Lanfermann, U. Pichlmeier, and M. Mehdorn, "Five-aminolevulinic acid for fluorescence-guided resection of recurrent malignant gliomas: a phase ii study," *Neurosurgery* **65**(6), 1070–1076; discussion 1076–1077 (2009).
50. U. Pichlmeier, A. Bink, G. Schackert, and W. Stummer, "Resection and survival in glioblastoma multiforme: an RTOG recursive partitioning analysis of ALA study patients," *J. Neuro-Oncol.* **10**(6), 1025–1034 (2008).
51. W. Stummer, H. J. Reulen, T. Meinel, U. Pichlmeier, W. Schumacher, J. C. Tonn, V. Rohde, F. Oppel, B. Turowski, C. Woiciechowsky, K. Franz, and T. Pietsch, "Extent of resection and survival in glioblastoma multiforme: identification of and adjustment for bias," *Neurosurgery* **62**(3), 564–576; discussion 564–576 (2008).
52. S. Utsuki, N. Miyoshi, H. Oka, Y. Miyajima, S. Shimizu, S. Suzuki, and K. Fujii, "Fluorescence-guided resection of metastatic brain tumors using a 5-aminolevulinic acid-induced protoporphyrin IX: pathological study," *Brain Tumor Pathol.* **24**(2), 53–55 (2007).
53. J. D. Johansson, "Spectroscopic method for determination of the absorption coefficient in brain tissue," *J. Biomed. Opt.* **15**(5), 057005 (2010).
54. P. V. Butte, B. K. Pikul, A. Hever, W. H. Yong, K. L. Black, and L. Marcu, "Diagnosis of meningioma by time-resolved fluorescence spectroscopy," *J. Biomed. Opt.* **10**(6), 064026 (2005).
55. A. N. Yaroslavsky, P. C. Schulze, I. V. Yaroslavsky, R. Schober, F. Ulrich, and H. J. Schwarzmaier, "Optical properties of selected native and coagulated human brain tissues in vitro in the visible and near infrared spectral range," *Phys. Med. Biol.* **47**(12), 2059–2073 (2002).
56. Z. Volynskaya, A. S. Haka, K. L. Bechtel, M. Fitzmaurice, R. Shenk, N. Wang, J. Nazemi, R. R. Dasari, and M. S. Feld, "Diagnosing breast cancer using diffuse reflectance spectroscopy and intrinsic fluorescence spectroscopy," *J. Biomed. Opt.* **13**(2), 024012 (2008).
57. S. C. Gebhart, W. C. Lin, and A. Mahadevan-Jansen, "In vitro determination of normal and neoplastic human brain tissue optical properties using inverse adding-doubling," *Phys. Med. Biol.* **51**(8), 2011–2027 (2006).
58. N. N. Boustany, S. A. Boppart, and V. Backman, "Microscopic imaging and spectroscopy with scattered light," *Annu. Rev. Biomed. Eng.* **12**, 285–314 (2010).
59. W. C. Lin, S. A. Toms, M. Motamedi, E. D. Jansen, and A. Mahadevan-Jansen, "Brain tumor demarcation using optical spectroscopy; an *in vitro* study," *J. Biomed. Opt.* **5**(2), 214–220 (2000).
60. R. F. Deighton, R. McGregor, J. Kemp, J. McCulloch, and I. R. Whittle, "Glioma pathophysiology: insights emerging from proteomics," *Brain Pathol.* **20**(4), 691–703 (2010).
61. S. Collaud, A. Juzeniene, J. Moan, and N. Lange, "On the selectivity of 5-aminolevulinic acid-induced protoporphyrin IX formation," *Curr. Med. Chem.* **4**(3), 301–316 (2004).
62. G. L. Semenza, "Targeting HIF-1 for cancer therapy," *Nat. Rev. Cancer* **3**(10), 721–732 (2003).
63. G. Bergers and L. E. Benjamin, "Tumorigenesis and the angiogenic switch," *Nat. Rev. Cancer* **3**(6), 401–410 (2003).
64. D. Liao and R. S. Johnson, "Hypoxia: a key regulator of angiogenesis in cancer," *Cancer Metastasis Rev.* **26**(2), 281–290 (2007).
65. D. J. Brat and T. B. Mapstone, "Malignant glioma physiology: cellular response to hypoxia and its role in tumor progression," *Ann. Intern. Med.* **138**(8), 659–668 (2003).
66. P. Carmeliet, "Mechanisms of angiogenesis and arteriogenesis," *Nat. Med.* **6**(4), 389–395 (2000).
67. J. T. Grier and T. Batchelor, "Low-grade gliomas in adults," *Oncologist* **11**(6), 681–693 (2006).

68. P. Rolfe, "*In vivo* near-infrared spectroscopy," *Annu. Rev. Biomed. Eng.* **2**, 715–754 (2000).
69. S. Srinivasan, B. W. Pogue, S. Jiang, H. Dehghani, C. Kogel, S. Soho, J. J. Gibson, T. D. Tosteson, S. P. Poplack, and K. D. Paulsen, "Interpreting hemoglobin and water concentration, oxygen saturation, and scattering measured in vivo by near-infrared breast tomography," *Proc. Natl. Acad. Sci. U.S.A.* **100**(21), 12349–12354 (2003).
70. O. Ivanciuc, "Applications of support vector machines in chemistry," *Reviews in Computational Chemistry*, K. B. Lipkowitz and T. R. Cundari, Eds., pp. 291–400, Wiley, New York (2007).